

Interferometry by deconvolution: Part 2 — Theory for elastic waves and application to drill-bit seismic imaging

Ivan Vasconcelos¹ and Roel Snieder²

ABSTRACT

Deconvolution interferometry successfully recovers the impulse response between two receivers without the need for an independent estimate of the source function. Here we extend the method of interferometry by deconvolution to multi-component data in elastic media. As in the acoustic case, elastic deconvolution interferometry retrieves only causal scattered waves that propagate between two receivers as if one acts as a pseudosource of the point-force type. Interferometry by deconvolution in elastic media also generates artifacts because of a clamped-point boundary condition imposed by the deconvolution process. In seismic-while-drilling (SWD) practice, the goal is to determine the subsurface impulse response from drill-bit noise records. Most SWD technologies rely on pilot sensors and/or models to predict the drill-bit source function, whose imprint is then removed from the data. Interferometry by deconvolution is of most use to SWD applications in which pilot records are absent or provide unreliable estimates of bit excitation. With a numerical SWD subsalt example, we show that deconvolution interferometry provides an image of the subsurface that cannot be obtained by correlations without an estimate of the source autocorrelation. Finally, we test the use of deconvolution interferometry in processing SWD field data acquired at the San Andreas Fault Observatory at Depth (SAFOD). Because no pilot records were available for these data, deconvolution outperforms correlation in obtaining an interferometric image of the San Andreas fault zone at depth.

INTRODUCTION

Interferometry is a proven methodology for recovering the impulse response between any two receivers. When measured data are

excited by correlated noise sources, results from crosscorrelation interferometry depend on the power spectrum of the source (Larose et al., 2006; Snieder et al., 2006; Wapenaar and Fokkema, 2006; Vasconcelos, 2007). As shown by Vasconcelos and Snieder (2008, hereafter called Part 1), interferometry also can be accomplished by deconvolution. One advantage of deconvolution interferometry, compared with its correlation counterpart, is that it removes the source function without the need for an extra processing step. The main objectives of this paper are to (1) extend the method of deconvolution interferometry to elastic media and (2) validate deconvolution interferometry as a method to recover impulse signals from drill-bit noise without the need for an independent estimate of the drill-bit excitation function.

Recordings of drilling noise can be used for seismic imaging (Rector and Marion; 1991). In most seismic-while-drilling (SWD) applications (e.g., Poletto and Miranda, 2004), data acquisition and imaging geometries fall under the category of reverse vertical seismic processing (RVSP) experiments, in which knowledge of the position of the drill bit is required. With the autocorrelogram migration method, Schuster et al. (2003) and Yu et al. (2004) recognize that interferometry could be applied to SWD data without any knowledge of drill-bit position. Poletto and Petronio (2006) use interferometry to characterize fault zones ahead of a tunnel being drilled. In the specific case of SWD applications, the drill-bit noise signal (and its power spectrum) is a long, complicated source-time function with a narrow-band signature (Poletto and Miranda, 2004). Hence, extracting an impulsive response from the application of crosscorrelation interferometry to SWD data requires an additional processing step: removing the source signature (Wapenaar and Fokkema, 2006).

There are many examples of successful applications of SWD technology. Most SWD methods rely on so-called pilot sensors to estimate independently the drill-bit excitation (Rector and Marion, 1991; Haldorsen et al., 1994; Poletto and Miranda, 2004). Without relying on pilot records, Miller et al. (1990) design multichannel weighting deconvolution filters based on statistical assumptions about the source function. Poletto and Miranda (2004) provide a

Manuscript received by the Editor 9 July 2007; revised manuscript received 19 November 2007; published online 9 May 2008.

¹Formerly Colorado School of Mines, Department of Geophysics, Center for Wave Phenomena; presently ION Geophysical, GXT Imaging Solutions, Egham, United Kingdom. E-mail: ivan.vasconcelos@iongeo.com.

²Colorado School of Mines, Department of Geophysics, Center for Wave Phenomena, Golden, Colorado, U.S.A. E-mail: rsnieder@mines.edu.

© 2008 Society of Exploration Geophysicists. All rights reserved.

comprehensive description of pilot deconvolution technologies. Some pilot-based SWD methods deconvolve bit excitation directly from recorded data (e.g., Haldorsen et al., 1994), although most methodologies rely on crosscorrelations (e.g., Rector and Marion, 1991; Poletto and Miranda, 2004). A close connection exists between correlation-based SWD methods and crosscorrelation interferometry, which we highlight in this paper.

Pilot-based SWD technologies can be elaborate. Sophisticated pilot recordings can use dual-field sensors (Poletto et al., 2004) or accelerometers mounted close to the drill bit (Poletto and Miranda, 2004). Recognizing that pilot records are imperfect estimates of drill-bit excitation, Poletto et al. (2000) present a statistical technique that further optimizes pilot deconvolution. As described by Poletto and Miranda (2004), examples of data for which pilot deconvolution can be unsuccessful are when the drill bit is inside deep, deviated wells or when the drill bit is below strong geologic contrasts (e.g., below salt).

Most SWD experiments involve RVSP geometries (Rector and Marion, 1991; Poletto and Miranda, 2004). Drilling noise also has been used for imaging ahead of the drill bit (i.e., look-ahead (VSP)) as shown by Armstrong et al. (2000) and Malusa et al. (2002). Armstrong et al. (2000) provide examples of drill-bit imaging in the deepwater Gulf of Mexico. Most SWD experiments are conducted onshore with roller-cone drill bits (Poletto and Miranda, 2004). Deepwater SWD is uncommon because pilot records yield poor representations of bit excitation in these conditions (Poletto and Miranda, 2004).

In this paper, we demonstrate the potential of interferometry by deconvolution for treating passive recordings of drilling noise in deepwater subsalt environments. We first extend acoustic concepts presented in Part 1 to elastic media, demonstrating how elastic scattered waves can be extracted by deconvolution interferometry. Next, we describe the role of deconvolution interferometry (Part 1) in extracting the impulse response between receivers from drilling noise. With a numerical example using the Sigsbee salt model, we compare the performance of deconvolution and correlation interferometry in passive drill-bit imaging. Finally, we present results of using deconvolution interferometry for imaging the San Andreas fault (SAF) zone from SWD data acquired at Parkfield, California.

ELASTIC DECONVOLUTION INTERFEROMETRY

Our goal is to design a deconvolution interferometry approach for elastic media that behaves similarly to one described in Part 1. With that objective, we define the following operation:

$$D_{AB}^{(p,q)} = D_{AB,K}^{(p,q)} = \frac{u_{(p,K)}^{(v,\Phi)}(\mathbf{r}_A, \mathbf{s}, \omega)}{u_{(q,K)}^{(v,\Phi)}(\mathbf{r}_B, \mathbf{s}, \omega)} = \frac{G_{(p,K)}^{(v,\Phi)}(\mathbf{r}_A, \mathbf{s}, \omega)}{G_{(q,K)}^{(v,\Phi)}(\mathbf{r}_B, \mathbf{s}, \omega)}, \quad (1)$$

where $u_{(p,K)}^{(v,\Phi)} = \mathcal{W}_K G_{(p,K)}^{(v,\Phi)}$ are measured responses in the frequency domain. The subscript p (or q) denotes a particular component of measured particle velocity (the superscript v indicates the measured field quantity is particle velocity). For brevity, we omit the dependence on angular frequency ω in all subsequent equations. To maintain consistency with Part 1, we describe the impulse response G as a superposition of direct waves G_0 and scattered waves G_S . As in Part 1, the results we present are not limited to this description, i.e., G_0 and G_S can be arbitrary unperturbed waves and wavefield perturbations, respectively. As in Wapenaar and Fokkema (2006), the superscript Φ indicates if the source is a P-wave source (for which $K = 0$)

or S-wave sources polarized in different directions ($K = 1, 2, 3$).

In equation 1, $D_{AB}^{(p,q)}$ is given by the summation of the four $D_{AB,K}^{(p,q)}$ terms over the source index K . Each $D_{AB,K}^{(p,q)}$ term is the deconvolution of the p th component of the receiver at \mathbf{r}_A with the q th component of the receiver at \mathbf{r}_B for a given source of type Φ . This value W_K is the Fourier transform of the source-time functions; this quantity can depend on the source location and source type. Note that the source function cancels in equation 1 in the same way as in the acoustic case (see Part 1, equation 9). This suggests that, as with its acoustic counterpart noted in Part 1, elastic deconvolution interferometry can suppress arbitrarily complicated excitation functions.

As in acoustic deconvolution interferometry, the denominator in equation 1 can be expanded in a power series when the scattered wavefield is weak compared with the direct wavefield. After expanding the denominator in equation 1, we get

$$\{G_{(q,K)}^{(v,\Phi)}(\mathbf{r}_B, \mathbf{s})\}^{-1} = \frac{1}{G_{0(q,K)}^{(v,\Phi)}(\mathbf{r}_B, \mathbf{s})} \times \sum_{n=0}^{\infty} (-1)^n \left(\frac{G_{S(q,K)}^{(v,\Phi)}(\mathbf{r}_B, \mathbf{s})}{G_{0(q,K)}^{(v,\Phi)}(\mathbf{r}_B, \mathbf{s})} \right)^n, \quad (2)$$

which we refer to as the elastic deconvolution interferometry series. This series expansion has the same form as the deconvolution interferometry series for acoustic media. Because the series in equation 2 has an interpretation analogous to that presented in equation 11 of Part 1, much of the discussion regarding acoustic deconvolution interferometry applies to the elastic case.

As with deconvolution interferometry in acoustic media, we use equation 2 in equation 1 and then integrate over the available sources \mathbf{s} , giving

$$\int_{\partial V_1} D_{AB,K}^{(p,q)} ds = \underbrace{\int_{\partial V_1} \frac{G_{0(p,K)}^{(v,\Phi)}(\mathbf{r}_A, \mathbf{s}) \{G_{0(q,K)}^{(v,\Phi)}(\mathbf{r}_B, \mathbf{s})\}^*}{|G_{0(q,K)}^{(v,\Phi)}(\mathbf{r}_B, \mathbf{s})|^2} ds}_{\text{Term 1}} + \underbrace{\int_{\partial V_1} \frac{G_{S(p,K)}^{(v,\Phi)}(\mathbf{r}_A, \mathbf{s}) \{G_{0(q,K)}^{(v,\Phi)}(\mathbf{r}_B, \mathbf{s})\}^*}{|G_{0(q,K)}^{(v,\Phi)}(\mathbf{r}_B, \mathbf{s})|^2} ds}_{\text{Term 2}} - \underbrace{\int_{\partial V_1} \frac{G_{0(p,K)}^{(v,\Phi)}(\mathbf{r}_A, \mathbf{s}) G_{S(q,K)}^{(v,\Phi)}(\mathbf{r}_B, \mathbf{s})}{\{G_{0(q,K)}^{(v,\Phi)}(\mathbf{r}_B, \mathbf{s})\}^2} ds}_{\text{Term 3}}; \quad (3)$$

where we keep only the terms whose integrands are linear in the scattered waves G_S . This equation is analogous to equation 13 in Part 1: terms 1, 2, and 3 have a similar meaning as terms D_{AB}^1 , D_{AB}^2 , and D_{AB}^3 . An important difference between terms in equation 3 and their acoustic counterparts is that each term in equation 3 is composed of four terms for $K = 0, 1, 2, 3$.

Following reasoning given for interpreting equation 13 in Part 1, $|G_{0(q,K)}^{(v,\Phi)}(\mathbf{r}_B, \mathbf{s})|^2$ are slowly varying functions of \mathbf{s} , and the source averaging effectively yields a constant for each value of K . The phase of integrands in equation 3 is controlled by the numerators (see Part 1). In equation 3, ∂V_1 is a surface segment (i.e., the source acquisition plane) that contains the stationary source locations that excite the desired waves in $G_{S(p,q)}^{(v,\Phi)}(\mathbf{r}_A, \mathbf{r}_B)$ (Vasconcelos, 2008; Vasconcelos and Snieder, 2008, Appendix A). By inspecting term 2 in equation 3, following equation A-9 in Appendix A, we conclude that

$$\int_{\partial V_1} \frac{G_{S(p,K)}^{(v,\Phi)}(\mathbf{r}_A, \mathbf{s}) \{G_{0(q,K)}^{(v,\Phi)}(\mathbf{r}_B, \mathbf{s})\}^*}{|G_{0(q,K)}^{(v,\Phi)}(\mathbf{r}_B, \mathbf{s})|^2} d\mathbf{s} \approx \mathcal{K} G_{S(p,q)}^{(v,f)}(\mathbf{r}_A, \mathbf{r}_B), \quad (4)$$

where \mathcal{K} is a constant related to the source averaging of spectra $|G_{0(q,K)}^{(v,\Phi)}(\mathbf{r}_B, \mathbf{s})|^2$.

Like the contribution D_{AB}^2 of Part 1, equation 4 shows that term 2 yields causal elastic scattered waves that propagate from \mathbf{r}_B to \mathbf{r}_A . Equation 4 states that scattered waves described by $G_{S(p,q)}^{(v,f)}(\mathbf{r}_A, \mathbf{r}_B)$ are excited by the p th component of the receiver at \mathbf{r}_B . As in the acoustic case (equation 15 of Part 1), the scattered waves that arise from term 2 in the second line of equation 3 are the objective of interferometry.

The interpretation of terms 1 and 3 in equation 3 also is analogous to their acoustic counterparts D_{AB}^1 and D_{AB}^3 (see Part 1). Because the unperturbed fields G_0 satisfy the elastic wave equation (Appendix A), term 1 (equation 3) results in causal and anticausal direct waves (after Wapenaar and Fokkema, 2006; Wapenaar, 2007). If receivers lie on a free surface, term 1 will also retrieve causal and anticausal surface waves, along with the direct arrivals. Term 3 is a spurious arrival that arises from a clamped-point boundary condition imposed by deconvolution interferometry. Its behavior is similar to that of D_{AB}^3 in Part 1, except that more arrivals are associated with P- and S-wave modes and mode conversions occur at the scatterers. Refer to Figure 1 of Part 1 for a description of paths defined by term 3 for a single scatterer.

In our elastic case, setting $\mathbf{r}_A = \mathbf{r}_B$ and $p = q$ in equation 1 results in $D_{BB,K}^{(q,q)} = 1$; this translates to the time-domain condition

$$D_{BB,K}^{(q,q)}(t) = \delta(t). \quad (5)$$

This condition does not hold if receivers at \mathbf{r}_B and \mathbf{r}_A measure different field quantities, e.g., one receiver measures stress but the other measures particle velocity. Equation 5 imposes a clamped-point boundary condition for the pseudosource experiment reconstructed by deconvolution interferometry. Although in the acoustic case point \mathbf{r}_B is completely clamped for $t \neq 0$ (see discussion in Part 1), in elastic media \mathbf{r}_B is fixed only in the q -direction for $t \neq 0$. This means all clamped-point scattered waves that depart from \mathbf{r}_B are excited by a pseudopoint force in the q -direction.

The intensity and orientation of this q -oriented pseudoforce is governed by the q -component of polarization of the wave incoming at \mathbf{r}_B . If the incoming wave does not have a polarization component in the q -direction, its interaction with \mathbf{r}_B does not produce a clamped-point scattered wave. On the other hand, if the incoming wave is polarized only in the q -direction, \mathbf{r}_B behaves as a perfect point scatterer. For a detailed discussion on multiple scattering caused by the clamped-point boundary condition in deconvolution interferometry, see Appendix B in Part 1.

In equations 1, 3, and 4, we perform a summation over a source index K , as in the approach by Wapenaar and Fokkema (2006). This assumes the three-component elastic responses are measured for all four source types: a P-wave source and three orthogonally oriented S-wave sources. In practice, such source configurations are seldom available, and the application is restricted typically to one source type. With only one source type available, the integral in equation 4 yields a partial reconstruction of $G_{S(p,q)}^{(v,f)}(\mathbf{r}_A, \mathbf{r}_B)$. In the case of single scattered waves reconstructed from the interference of transmission and reflection responses (such as data examples provided in this pa-

per), the partial reconstruction of $G_{S(p,q)}^{(v,f)}(\mathbf{r}_A, \mathbf{r}_B)$ by the use of equation 4 yields events with correct kinematics but distorted amplitudes (Draganov et al., 2006). A thorough discussion of the contribution of different source types, as well as the effects of not having all source types for elastic interferometry, is given in Draganov et al. (2006).

DRILL-BIT SEISMIC IMAGING AND DECONVOLUTION INTERFEROMETRY

The frequency-domain wavefield measured at \mathbf{r}_A excited by a working drill bit at \mathbf{s} is given by

$$u(\mathbf{r}_A, \mathbf{s}) = W(\mathbf{s})G(\mathbf{r}_A, \mathbf{s}), \quad (6)$$

where G is the impulse response between \mathbf{s} and \mathbf{r}_A and where $W(\mathbf{s})$ is the drill-bit excitation function. For simplicity, we use scalar quantities to address the role of deconvolution interferometry in drill-bit imaging, although the field-data example we discuss later uses the elastic formulation described previously.

As in most exploration-imaging experiments, the objective of drill-bit seismology is to image the subsurface from its impulse response G that needs to be obtained from equation 6. The main issue for successful imaging from drill-bit noise is removing the imprint of the source function W (Rector and Marion, 1991; Haldorsen et al., 1994; Poletto and Miranda, 2004). The first complication imposed by drill-bit excitation is that the source is constantly active. In other words, the source pulse is of equal length to the recording time of the data. Additionally, the drill bit is a source of coherent noise that is dominated by specific vibrational modes associated with the drilling process (Poletto, 2005a). These resonant modes associated with drilling give the time-domain drill-bit signature a monochromatic character. Apart from coherent vibrations, weaker random vibrations that occur during drilling render the drill-bit signal more wide-band (Poletto, 2005a). We illustrate these issues in our synthetic example, in which we use a numerical model for the drill-bit excitation.

Current interferometric approaches to processing drill-bit noise records rely on correlations (e.g., Schuster et al., 2003; Poletto and Miranda, 2004; Yu et al., 2004). The crosscorrelation of wavefields measured at \mathbf{r}_A and \mathbf{r}_B is, in the frequency domain, given by

$$C_{AB} = u(\mathbf{r}_A, \mathbf{s})u^*(\mathbf{r}_B, \mathbf{s}) = |W(\mathbf{s})|^2 G(\mathbf{r}_A, \mathbf{s})G^*(\mathbf{r}_B, \mathbf{s}), \quad (7)$$

where the asterisk stands for complex conjugation. The crosscorrelation thus is influenced by the power spectrum $|W(\mathbf{s})|^2$ of the drill-bit source function. In the time domain, the power spectrum in equation 7 corresponds to the autocorrelation of the drill-bit source-time function. This autocorrelation, despite being zero phase, often is a long, complicated waveform with a monochromatic character.

In most drill-bit processing methods, removal of the drill-bit source function in equation 6 (or of its autocorrelation, equation 7) relies on an independent estimate of drill-bit excitation. This estimate comes typically in the form of the so-called pilot record or pilot trace (e.g., Rector and Marion, 1991; Poletto and Miranda, 2004). The pilot records are data acquired by accelerometers placed in the rig/drillstem structure. Within literature on SWD, there are different descriptions of the signal acquired by pilot sensors. Most of these descriptions are based on deterministic physical models for wave propagation in the rig/stem/bit system (Rector, 1992; Rector and Hargage, 1992; Haldorsen et al., 1994; Poletto and Miranda, 2004). Poletto et al. (2000) and Poletto and Miranda (2004) propose a statistical approach to describe the drill-bit signal.

Because, for the purpose of deconvolution interferometry, we do not require a particular description of the pilot signal, it is convenient to express it in the general form

$$P(\mathbf{r}_d, \mathbf{s}) = W(\mathbf{s})T_d(\mathbf{r}_d, \mathbf{s}), \quad (8)$$

where T_d is the transfer function of the drillstem and rig assembly and \mathbf{r}_d is the location of the pilot sensor in the assembly. This transfer function includes reflection and transmission coefficients of the rig/stem/bit system, drillstring multiples, etc. (Poletto and Miranda, 2004).

The autocorrelation of the pilot signal in equation 8 gives

$$C_{PP} = |W(\mathbf{s})|^2 |T_d(\mathbf{r}_d, \mathbf{s})|^2. \quad (9)$$

From this autocorrelation and with additional knowledge about T_d , it is possible to design a filter \mathcal{F} of the form

$$\mathcal{F}_{C_{PP}} \approx \frac{1}{|W(\mathbf{s})|^2}. \quad (10)$$

We use $\mathcal{F}_{C_{PP}}$ to indicate that \mathcal{F} is a function of autocorrelation C_{PP} . The deterministic (Rector, 1992; Rector and Hardage, 1992; Halvorsen et al., 1994; Poletto and Miranda, 2004) or statistical (Poletto et al., 2000; Poletto and Miranda, 2004) descriptions of T_d aim to remove its influence (equation 8) in the design of filter \mathcal{F} .

We present \mathcal{F} as an approximation to $|W(\mathbf{s})|^{-2}$ in equation 10 because the theories used to eliminate the influence of T_d are approximate (e.g., Rector and Hardage, 1992; Poletto and Miranda, 2004). Multiplying filter \mathcal{F} (equation 10) by the crosscorrelation in equation 7 gives

$$\mathcal{F}_{C_{PP}} C_{AB} \approx G(\mathbf{r}_A, \mathbf{s}) G^*(\mathbf{r}_B, \mathbf{s}). \quad (11)$$

According to equation 11, \mathcal{F} removes the power spectrum of the drill-bit excitation from the correlation in equation 7. Application of \mathcal{F} is what is referred to as pilot deconvolution (Poletto and Miranda, 2004). The SWD RVSP methods rely on the crosscorrelations of

geophone data (equation 6) with the pilot signal (equation 8) to determine the time delay of waves that propagate between the drill bit and receivers (e.g., Rector and Marion, 1991; Poletto and Miranda, 2004). For these methods, it is necessary to know the drill-bit position \mathbf{s} .

There are different approaches to processing SWD data. Most of them rely on crosscorrelation (e.g., Rector and Marion, 1991; Poletto and Miranda, 2004). Some correlation-based processing techniques (e.g., RVSP techniques) require knowledge of \mathbf{s} and apply pilot deconvolution in a manner similar to that of equations 10 and 11. Another approach to treating drilling noise records is to use a source average of the crosscorrelations (Schuster et al., 2004; Poletto and Miranda, 2004; Yu et al., 2004), which are similar to correlation-based interferometry (e.g., Bakulin and Calvert, 2006; Wapenaar and Fokkema, 2006).

Although we describe SWD processing by the correlation of recordings made by geophones at two arbitrary locations \mathbf{r}_A and \mathbf{r}_B , some SWD applications rely on correlations between pilot and geophone signals (Poletto and Miranda, 2004). Methods based on pilot trace correlations are affected by the drill-bit source function in the same way it affects methods based on geophone correlations. Therefore, our pilot deconvolution discussion also applies to SWD processing by correlating pilot and geophone traces (Poletto and Miranda, 2004).

Role of deconvolution interferometry

Following the theory and examples presented, using deconvolution interferometry (e.g., equations 1 and 3 or equations 9 and 13 from Part 1 for the acoustic case) to process SWD data does not require an independent estimate of the drill-bit source function. This is the first and main difference between deconvolution interferometry and most correlation-based methods used in SWD data processing. Apart from being an alternative method for treating data from standard SWD experiments, interferometry by deconvolution would be particularly useful when pilot records are unavailable or are poor estimates of the drill-bit excitation function. Poletto and Miranda (2004) provide examples of pilot recordings that give unreliable estimates of the drill-bit source function. This is the case when transmission along the drill string is weak, when the drill bit is deep (on the order of several thousands of feet), when the well is deviated, or when two or more nearby wells are drilling simultaneously with the well equipped with pilot sensors.

As in interferometry methods based on correlation (Schuster et al., 2003; Yu et al., 2004), knowledge of \mathbf{s} is not necessary for processing SWD data by deconvolution interferometry. The only requirement is that the drill bit occupy the stationary source locations that give rise to targeted scattered waves propagating between the receivers (Snieder et al., 2006; Vasconcelos, 2007). Analogous to the method proposed by Schuster et al. (2003) for imaging drill-bit noise, it is possible to use deconvolution interferometry to reconstruct primary arrivals from free-surface ghost reflections.

SUBSALT NUMERICAL EXAMPLE

The drill-bit imaging numerical experiment we present is conducted with the 2D Sigsbee salt model (Figure 1). In this example, we place a long 100-receiver downhole array below the salt canopy in a 45° deviated well. The first receiver is placed at $x = 14,630$ m and $z = 4877$ m, and the last receiver is at $x = 16,139$ m and $z = 6385$ m. Receivers are spaced evenly; x and z translate to the lat-

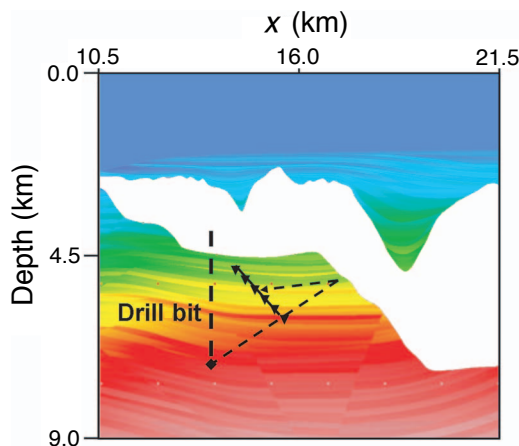


Figure 1. Structure of Sigsbee model and schematic acquisition geometry of the drill-bit experiment. Colors in the model denote acoustic wave speed. The dashed black line indicates a well being drilled, which excites waves in the medium. Waves are recorded in a deviated instrumented well, inclined at 45° with respect to the vertical direction. The solid line with triangles represents the instrumented well. The dashed arrow illustrates a stationary contribution to singly reflected waves that can be used to image the salt flank from drilling noise.

eral and depth coordinates in Figure 1, respectively. The borehole array records drilling noise from a vertical well placed at $x = 14,478$ m (Figure 1). The drill-bit noise is recorded for a drill-bit depth interval that ranges from $z = 4572$ m to 6705 m. The objective of this numerical experiment is to show that deconvolution interferometry can recover, from drill-bit noise, upgoing single-scattered waves that propagate between receivers, such as the one represented by the raypath in Figure 1 (dashed arrow). The upgoing single-scattered waves recovered by interferometry of drill-bit noise can be used to image the Sigsbee structure from below.

To simulate drill-bit wave excitation in the numerical experiment, we first modeled 200 evenly spaced shots within the drilling interval of interest. These shots were modeled by an acoustic finite-difference method (Claerbout, 1985). Next, we convolved the shots with a 60-s model of drill-bit excitation (Figure 2). The model for drill-bit excitation is a roller-cone bit (Poletto, 2005a). We add band-limited noise (see Figure 2) using the noise model of Poletto and Miranda (2004) to increase the bandwidth of the drill-bit signal. The bit and drilling parameters used in our model are listed in the caption of Figure 2.

Figure 2a shows the power spectrum of the modeled bit signal; Figure 2b shows a portion of the drill-bit source function in the time domain. As discussed previously, the time-domain drill-bit excitation has a narrow-band character (Figure 2b) because the source power spectrum is dominated by vibrational drilling modes (Poletto and Miranda, 2004; Poletto, 2005a). The common-receiver gather from receiver 50 in Figure 3a shows that simulated data are dominated by the character of the drill-bit excitation function (Figure 2b). Records in Figure 3a depict a moveout that characterizes the direct-wave arrival from the drill bit. The weak events with positive slopes in the left-hand portion of Figure 3a are salt-bottom reflections from when the drill bit is close to the bottom of the salt (see geometry in Figure 1).

Interferometry of recorded data, such as in Figure 3a, result in pseudoshot gathers as in Figure 3b and c. The use of deconvolution interferometry (see Part 1) for a pseudosource placed at receiver 50 results in Figure 3b. The pseudoshot gather in Figure 3c is obtained from correlation interferometry (e.g., Draganov et al., 2006) for the same geometry as Figure 3b. Figure 3b and c represents waves excited by a pseudosource at receiver 50; however, the wavefield in Figure 3b is approximately impulsive, and the data in Figure 3c are dominated by the autocorrelation of the drill-bit source function. Because the excitation function is canceled in deconvolution interferometry (see Part 1), the pseudosource in Figure 3 is impulsive. The source power spectrum in equation 7 results, in the time domain, in the dominant reverberation in the pseudoshot generated by correlation (Figure 3c).

Many features of the deconvolution pseudoshot gather in Figure 3b are explained in Part 1. The interferometric shot gather generated by deconvolutions shows causal and acausal direct waves, and causal scattered arrivals. As discussed in Part 1, the zero-offset trace obtained by deconvolution interferometry is a band-limited delta function at $t = 0$. This also can be observed in Figure 3 for the trace at receiver 50 (i.e., the zero-offset trace). The presence of this delta function at zero offset imposes the so-called clamped-point boundary condition in acoustic media (see Part

1). Because of this boundary condition, the gather in Figure 3 contains spurious arrivals. Visual identification of these arrivals in the gather is not straightforward because the recorded wavefield is complicated, given the model's complexity (Figure 1). The effect of these spurious arrivals on images made from data reconstructed by deconvolution interferometry is discussed in Appendix B of Part 1.

Given the acquisition geometry in this numerical experiment (Figure 1), there is a point to the left-hand side of the receivers where the drill-bit position aligns with array direction. This drill-bit position samples a stationary source point for the direct waves that travel downward between receivers. These waves are responsible for recovering direct-wave events with positive slopes in Figure 3. With the drilling geometry shown in Figure 1, the drill bit never reaches a position where it aligns with the receivers to the right-hand side of the array. Therefore, the drill bit does not sample a stationary source point that emits waves that travel upward along the receiver array. Hence, the direct-wave events with negative slopes in the pseudoshot gather (Figure 3b) have a distorted curved moveout instead of the correct linear moveout shown by direct waves that have positive slopes.

We generate interferometric shot gathers such as those in Figure 3b and c for pseudosources at each receiver in the array. This yields

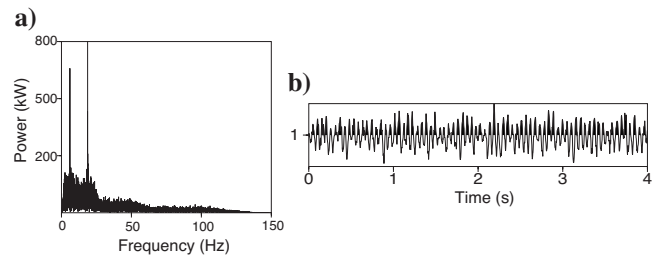


Figure 2. Numerical model of drill-bit excitation. (a) The power spectrum of the drill-bit source function. Although it is wide band, the power spectrum of the source function has pronounced peaks that correspond to vibrational drilling modes. (b) The drill-bit source function in the time domain. We show only the first 4 s of the 60-s drill-bit source function used in the modeling. The assumed drill bit is a tricone bit with 0.35 m OD, 0.075-m ID, and density of 7840 kg/m³. Each cone is composed of three teeth rows, as in the example by Poletto and Miranda (2004). Drillstring P-wave velocity is 5130 m/s. The drilling was modeled with a weight on bit of 98 kN, torque on bit of 6 kNm, 60 bit revolutions per minute, penetration rate of 10 m/hour, and four mud pumps with a rate of 70 pump strikes per minute.

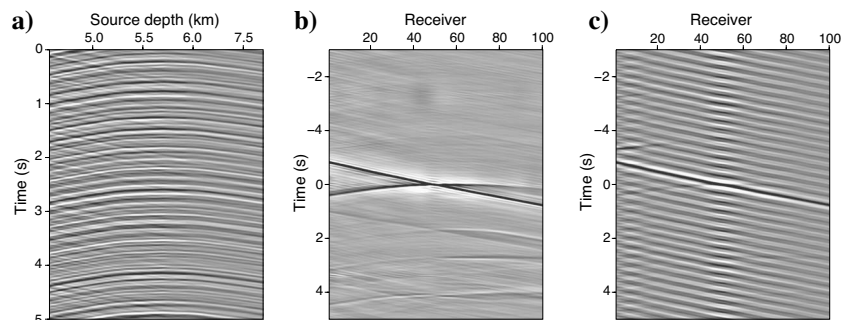


Figure 3. (a) Synthetic drill-bit noise records at receiver 50. Only 5 s of the 60 s of recording time are shown. The narrow-band character of the records is because of specific frequencies associated with the drilling process (Figure 2a). (b) Deconvolution-based interferometric shot gather with the pseudosource located at receiver 50. (c) Pseudoshot gather resulting from crosscorrelation with the same geometry as (b). Receiver 1 is the shallowest receiver of the borehole array (Figure 1).

100 pseudoshots, which are recorded by the 100-receiver array. We use shot-profile wave-equation migration to image the interferometric data. Migration is done by wavefield extrapolation with the split-step Fourier method. Wavefield extrapolation is done in a rectangular grid conformal to the receiver array, in which extrapolation steps are taken in the direction perpendicular to the array. Figure 4 displays images obtained from migrating the pseudoshot gathers from deconvolution interferometry (Figure 4a) and from the correlation-based method (Figure 4b). We explicitly choose not to correct for the effect of the drill-bit source function in the correlation image (Figure 4b) to simulate the condition in which an independent measure of the source excitation function is not available.

In interferometric experiments, the image aperture is dictated by the geometry of the receiver array (red lines in Figure 4). The position of physical sources used in interferometry, along with medium properties, controls the actual subsurface illumination achieved by interferometry. When sources surround receivers completely, the interferometric pseudosource radiates energy in all directions, much like a real physical source (Larose et al., 2006; Wapenaar and

Fokkema, 2006). When the physical excitation generated by sources is one-sided (Vasconcelos, 2007; Wapenaar, 2006), pseudosource radiation is uneven. In our case, the illumination given by interferometric shots differs from that obtained by placing real physical sources at the receiver locations. Hence, the resulting image from these active shots would be different, in terms of illumination, from those in Figure 4. This is an important distinction between imaging interferometric pseudoshots and imaging actual shots placed at receiver locations.

A comparison of images in Figure 4 with the Sigsbee model in Figure 1 shows that the image from deconvolution interferometry (Figure 4a) represents the subsurface structure better than the image from correlation interferometry (Figure 4b). Salt reflectors (top and bottom) are better resolved in Figure 4a than in Figure 4b. In addition, it is possible to identify subsalt sediment reflectors in Figure 4a, which are not visible in Figure 4b. Reflectors in Figure 4a are well resolved because deconvolution interferometry successfully suppresses the drill-bit source function when generating pseudoshot gathers (Figure 3). The image from deconvolution interferometry does not present severe distortions because of the spurious arrivals characteristic of deconvolution pseudoshot gathers.

As discussed in Part 1, deconvolution-related spurious events typically do not map onto coherent reflectors on shot-profile migrated images such as the one in Figure 4a. The image from correlation interferometry (Figure 4b) portrays a distorted picture of the Sigsbee structure (Figure 1) because the correlation-based pseudoshot gathers are dominated by the power spectrum of the drill-bit excitation (Figure 3c; equation 7). The narrow-band character of the drill-bit source (Figures 2b and 3a and c) is responsible for the ringed appearance of Figure 4b.

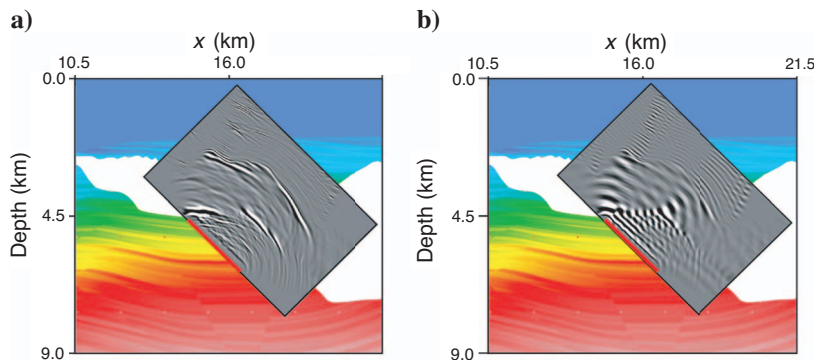


Figure 4. Images obtained from drill-bit noise interferometry. Images (in gray) are superposed on the Sigsbee model in Figure 1. (a) The image obtained from shot-profile wave-equation migration of pseudoshot gathers generated from deconvolution interferometry (as in Figure 3b). (b) The result of migrating correlation-based interferometric shot gathers. Red lines in the images represent the receiver array.

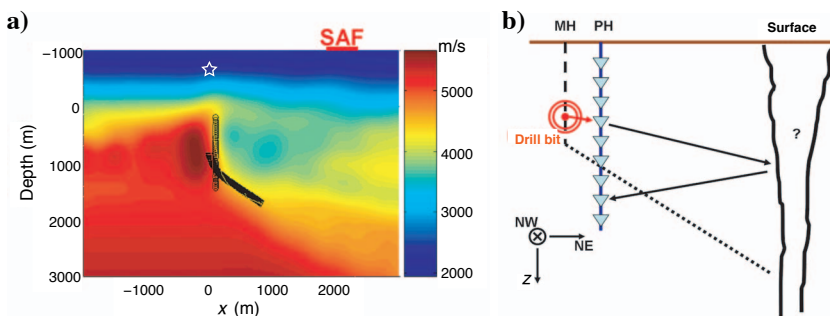


Figure 5. Southwest to northeast (left to right) cross sections at Parkfield. (a) The large-scale structure of the P-wave velocity field (velocities are color coded) at Parkfield, California. Circles indicate the location of sensors of the SAFOD pilot-hole array used for recording drilling noise. The SAFOD main hole is denoted by triangles. The location of the SAFOD drill site is depicted by the star. Depth is with respect to sea level. The altitude at SAFOD is approximately -660m . (b) The schematic acquisition geometry of the down-hole SWD SAFOD data set. Receivers are indicated by light blue triangles. Structures outlined by solid black lines to the right side of the figure represent a target fault. As indicated, receivers are oriented in the z - (or downward vertical), northeast, and northwest directions. (b) Schematic stationary path between the drill bit and two receivers. MH = main hole; PH = pilot hole.

SAFOD DRILL-BIT DATA

The San Andreas Fault Observatory at Depth (SAFOD) is located at Parkfield, California. Its objective is to study the San Andreas Fault (SAF) zone from borehole data and to monitor fault-zone activity. SAFOD consists of two boreholes: the pilot hole and the main hole. The geometry of the holes, relative to the surface trace of the SAF, is displayed in Figure 5a. Data we analyze consist of recordings of noise excited by drilling the main hole, recorded by the 32-receiver array placed permanently in the pilot hole.

The main objective of the SAFOD borehole-SWD experiment is to provide broadside illumination of the SAF that is impossible from surface measurements. Figure 5b illustrates how single reflections from the SAF may be recovered by drilling-noise records measured at the SAFOD pilot-hole array. The stationary path, indicated by red and black arrows in Figure 5b, shows that the interference between the drill-bit direct arrivals with fault-scattered waves can be used to reconstruct primary fault reflections propagating between receivers. Because the distance between

main and pilot holes is only on the order of 10 m (Boness and Zock, 2006), the drill bit offers only stationary contributions to waves emanating from a given receiver when drilling next to that receiver. The geologic context of this experiment and the full interpretation of results we show here, along with active-shot seismic data, are presented in Vasconcelos et al. (2007).

Because of field instrumentation issues (S. T. Taylor, 2006, personal communication), most data recorded by the pilot-hole array before July 15 are dominated by electrical noise. A window of approximately 20 hours prior to the intersection of the pilot hole by the main hole coincides with the portion of the pilot-hole data for which the instrumentation problem was fixed. According to main-hole drilling records, the depth interval sampled by the usable drill-bit data extends from approximately 350 to 450 m (in the scale in Figure 5a).

We use data recorded in this interval to generate interferometric shot records. Within the 350–450-m bit interval, the drill bit passes by pilot-hole receiver 26. Because the stationary contributions of the sources to recovering primary reflections from the SAF occur only when the roller-cone bit is next to a receiver, only receiver 26 can be used as a pseudosource for the deconvolution interferometry. Hence, \mathbf{r}_B in equation 1 is given by coordinates of receiver 26. So out of the 32 receivers of the SAFOD pilot-hole array, it is only possible to create interferometric shot gathers with a pseudosource at receiver 26.

A small portion of recorded data are shown in Figure 6. Data in Figure 6a are from the vertical component of receiver 26; data in Figure 6b and c correspond to receiver 23. Because traces shown in Figure 6 are subsequent drill-bit noise records of 1-minute duration (of which only the first 3 s are shown in Figure 6), the drill-bit position for records in the figure is practically constant. Data recorded by receiver 26 (Figure 6a) are low-pass filtered to preserve the signal as much as 75 Hz. A similar filter, preserving frequencies as much as 55 Hz, is applied to the original data from receiver 23 in Figure 6b, resulting in the data in Figure 6c. Data recorded by receiver 23 (Figure 6b) is heavily contaminated by electrical noise at 60, 120, and 180 Hz. This electrical noise is practically negligible in data from receiver 26, as shown by Figure 6a in which the 60-Hz oscillation cannot be seen. After low-pass filtering, data from receiver 23 (Figure 6c) shows a character similar to that from receiver 26 (Figure 6a).

A critical issue with processing SAFOD SWD data is that pilot records are not available. Therefore, pilot-based SWD processing (Rector and Marion, 1991; Haldorsen et al., 1994; Poletto and Miranda, 2004) cannot be applied to pilot-hole drill-bit data. Thus, these data are natural candidates for deconvolution interferometry. Figure 7 shows four pseudoshot gathers derived from deconvolution interferometry using different combinations of receiver components (see equations 1–4). We display traces for receivers 15–32 in

Figure 7 because electric noise in receivers 1–14 prevents the recovery of coherent signals. Before computing the pseudoshots in Figures 7 and 8, all data were low-pass filtered to preserve frequencies as high as 55 Hz. For the interferometry, we divide each minute-long record into two 30-s traces. With approximately 20 hours of recording time, the resulting traces in the pseudoshot records are the result of stacking on the order of 2000 deconvolved or correlated traces. For a discussion on our numerical implementation of deconvolution, see Appendix B.

Figure 7 shows that combining different components in deconvolution interferometry yields different waveforms. Scattered arrivals, indicated by red arrows, can be identified in Figure 7a and b but not in Figure 7c and d. The first reason for the difference between results

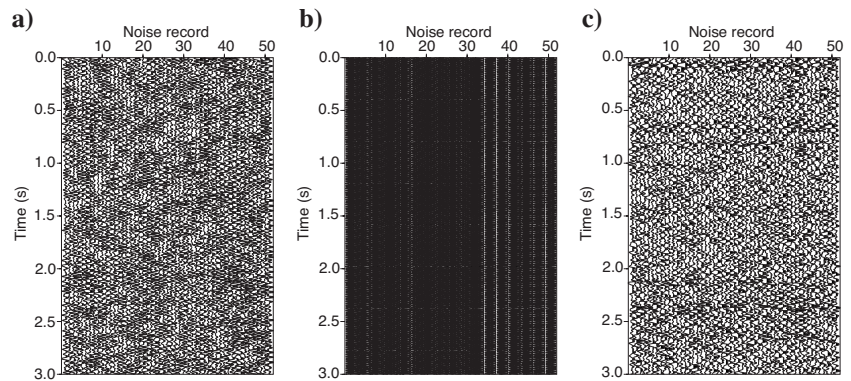


Figure 6. Drill-bit noise records from the SAFOD pilot hole. (a) Because the drill bit is closest to receiver 26, data recorded at this receiver are not contaminated by electrical noise. (b) Data recorded at receiver 23 for the same drill-bit positions. (c) Result of filtering the electrical noise from data in (b). These data show the first 3 s of the full records (which are 60 s long). For records shown here, the drill-bit position is practically constant. The data are from the vertical component of recording.

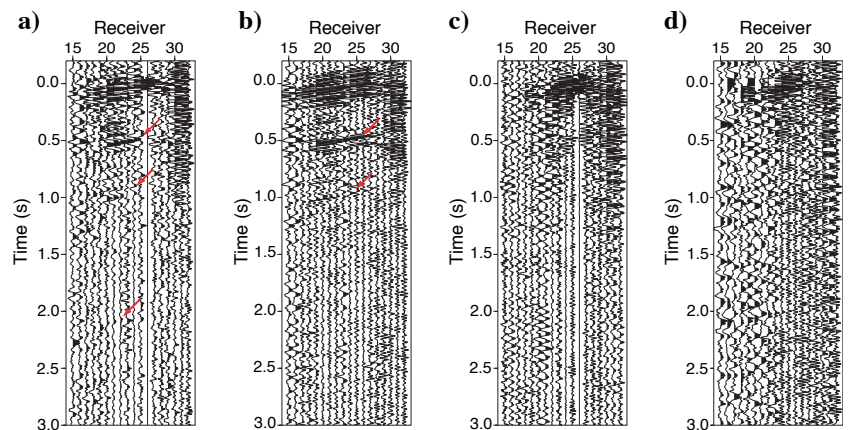


Figure 7. Pseudoshot gathers from deconvolution interferometry. In these gathers, receiver 26 acts as a pseudosource. Each panel is the result of deconvolving different combinations of receiver components: (a) deconvolution of z with z components; (b) z with northeast components; (c) northeast with northeast components; (d) northwest with z -components. Physically, (a) shows waves recorded by the vertical component for a pseudoshot at receiver 26, excited by a vertical point force. View (b) is the vertical component for a pseudoshot at PH 26. Unlike the wavefield in (a), it represents waves excited by a point force in the northeast direction. View (c) pertains to both excitation and recording in the northeast direction, whereas waves in (d) are excited by a vertical point-force and are recorded in the northwest direction. Red arrows show reflection events of interest. Note that receiver 32 is the shallowest receiver in SAFOD pilot-hole array (Figure 5). Receiver spacing is 40 m. Component orientations used here are the same as in Figure 5b.

in the four panels lies in equations 1–3. According to these equations, deconvolving data recorded in the p -component with data recorded by the q -component results in the interferometric impulse response recorded by the p -component and excited by the q -component. The caption of Figure 7 addresses corresponding the orientation of the recording and pseudoexcitation.

Radiation characteristics of the pseudosource, along with a signal-to-noise ratio (S/N) in different recording components of the receiver away from the drill bit (and from receiver 26), also are responsible for the differences in Figure 7. Because Figure 7b shows coherent events (red arrows) reconstructed from energy recorded by the northeast component, it follows that the direct-wave response from bit excitation has a nonzero polarization component in the northeast direction as well. In these data, receiver 26 records drill-bit direct waves polarized in the z - and northeast directions because the receiver is in the drill bit's near-field (the pilot hole and main hole are a few meters apart). The measured near-field response to an excitation in the z -direction (drilling direction is close to vertical) is polarized in the vertical and in-plane horizontal components (Aki and Richards, 1980; Tsvankin, 2001). Waves scattered from the SAF have far-field polarization because the fault zone is approximately 2 km away from the pilot hole. The lack of scattered signals in Figure 7c and d are mostly because of poor S/N in the northeast and northwest components of the receivers far from the drill bit.

Pseudoshot gathers in Figure 7 are generated by deconvolution interferometry, whereas gathers in Figure 8 are the result of correlation interferometry (e.g., Wapenaar, 2004; Draganov et al., 2006). Analogous to observations made earlier, the correlation-based interferometric shot gathers (Figure 8) are imprinted with the autocorrelation of the drill-bit source function, giving them a ringy appearance. Scattered events in Figure 7a and b cannot be identified in Figure 8a and b. The zero-offset trace (at receiver 26) in Figure 7a and c is a band-limited delta function centered at $t = 0$. This demonstrates the deconvolution interferometry boundary condition in equation 5. In Figure 7a, we do not observe pronounced spurious arrivals associated with the scattered events (marked by red arrows).

Along with geologic information from main-hole data and with an active shot acquired by sensors in the main hole, Vasconcelos et al. (2007) associate the event arriving with a zero-offset time of approx-

imately $t = 1.0$ s (second arrow from top) in Figure 7a and b to the primary P-wave reflection from the SAF. The event at 0.5 s (top arrow) could be the reflection from a blind fault zone intercepted by the SAFOD main hole (Boness and Zoback, 2006; Solum et al., 2006). The bottom arrow in Figure 7a indicates an event with a zero-offset time of approximately 2.0 s whose slope is consistent shear-wave velocity. We interpret this arrival as a pure-mode shear-wave reflection from the SAF. Because only the pseudoshots in Figure 7a and b present physically meaningful arrivals, we show only migrated images from these two panels.

Generally, drillstring multiples (Poletto and Miranda, 2004) should not present a problem to data reconstructed from receivers that lie far from the drillstring. This is not the case for SAFOD data because the pilot hole is only a few meters away from the drillstring, so the drillstring multiples in this case can be part of the wavefield that propagates between receivers. Our interpretation of events in Figure 7 is prone to error because drill-bit data might be contaminated by drillstring multiples. We do not account for drillstring multiples in our processing, so it is possible that some events in Figure 7 arise from such multiples.

Pseudoshot data were migrated with the same methodology as in the Sigsbee numerical example. We use shot-profile migration by wavefield extrapolation, in which the extrapolation steps are taken in the horizontal coordinate away from the SAFOD pilot hole (Figure 5). Migrated images are shown in Figure 9. Images of pseudoshots from deconvolution interferometry (left panels) show reflectors that cannot be identified in images from correlation interferometry (right panels). Images from correlation-based pseudoshots have a narrow-band character similar to the pseudoshots themselves, caused by the presence of the autocorrelation of the drill-bit excitation function (Figure 8). This is the same phenomenon we show in images from the Sigsbee model (Figure 4), except that Sigsbee images are produced from 100 pseudoshots. Because the SAFOD images result from migrating a single shot, reflectors are curved toward edges of the images (top and bottom of images in Figure 9) because of the direction-limited migration operator and relatively small aperture of the receiver array used to reconstruct the data.

The final image from the SAFOD SWD data was obtained by stacking the top images with the bottom ones in Figure 9. We do this to enhance reflectors that are common in both images. The final SAFOD images are shown in Figure 10. Figure 10 shows only the portion of images that yield physically meaningful reflectors, highlighted by yellow rectangles in Figure 9a and c. The image from deconvolution interferometry (Figure 10a) reveals reflectors that cannot be seen in the image from correlation interferometry (Figure 10b).

To interpret results from the interferometric image in Figure 10a in relation to the structure of the SAF, we superpose it on the SAF image from Chavarria et al. (2003) in Figure 11. Their image was generated from surface seismic data along with seismic and microseismic events from the SAF, measured at the surface and in the pilot hole. In Figure 11, we observe that the deconvolution-based interferometric image shows a prominent reflector (red arrow 2), consistent with the surface trace of the SAF. This is the reflector at $x \approx 2000$ m, indicated by the right arrow in Figure

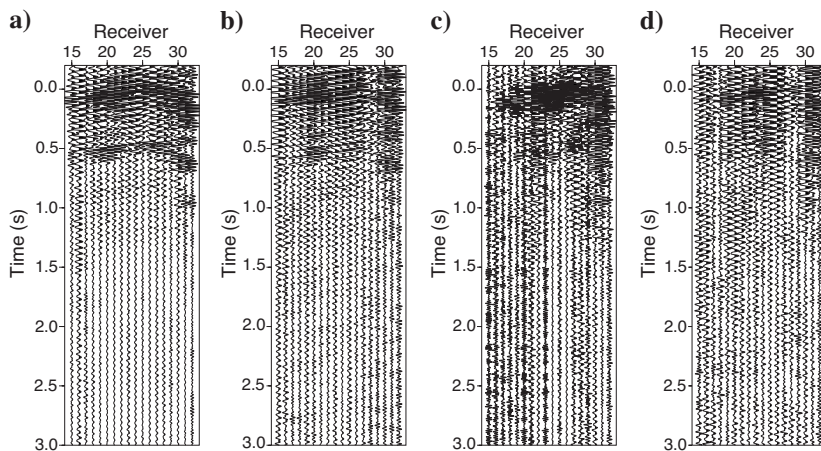


Figure 8. Pseudoshot gathers from correlation interferometry. Each panel is associated with the correlation of the same receiver components as in the corresponding panels in Figure 7. The physical interpretation of excitation and recording directions is the same as for Figure 7. Unlike data in Figure 7, the source function in these data is given by the autocorrelation of the drill-bit excitation.

10a. We argue (see also Vasconcelos et al., 2007) that this reflector coincides with the SAF's contact with metamorphic rocks to the northeast.

Events indicated by red arrows 1 and 4 in Figure 11 are interpreted to be artifacts, possibly because of drillstring multiples and improperly handled converted-wave modes (Vasconcelos et al., 2007). Event 3 is the reflector at $x \approx 1600$ m, marked by the left red arrow in Figure 10a. This reflector is interpreted to be a blind fault at Parkfield because it is imaged consistently by a separate active-shot VSP survey (Vasconcelos et al., 2007). The presence of this blind fault has been confirmed by its intersection with the main hole (Boness and Zoback, 2006; Solum et al., 2006).

DISCUSSION

In elastic media, the interferometric response obtained by deconvoluting the p -component of a given receiver by the q -component of another receiver results in scattered waves that propagate between these two receivers. These waves are the impulse response from a q -oriented point-force excitation at one of the receivers, recorded by the p -component at the other receiver. This is only true when P-wave and three-component S-wave sources are available. In most real-life experiments, this multiple source requirement is typically not met; hence, interferometry (by either deconvolution or crosscorrelation) yields an incomplete reconstruction of elastic waves propagating between receivers (Draganov et al., 2006). Moreover, as with the case of acoustic media, elastic deconvolution interferometry introduces artifact arrivals because of the clamped-point boundary condition. A discussion of the effect of these arrivals in imaging is provided in Appendix B of Part 1.

Because the deconvolved data satisfy the same wave equation as the original physical experiment, radiation properties of the drill bit (Poletto, 2005a) determine the radiation pattern of the pseudosource synthesized by interferometry (assuming all possible component combinations are used for interferometry). In the case of receivers positioned far from the drill bit and for highly heterogeneous media, deconvolution interferometry potentially can extract a response that is closer to a full elastic response because of multiple scattering (i.e., that results in equipartitioning), as discussed by Wapenaar and Fokkema (2006) and Snieder et al. (2007). When the conditions for equipartitioning (Snieder et al., 2007; Vasconcelos, 2007) are satisfied, our formulation can be used to design elastic pseudosources by deconvolution interferometry with varying radiation patterns according to the chosen point-force orientation.

Our numerical experiment with the Sigsbee model seeks to reproduce a passive subsalt SWD experiment in the absence of pilot recordings. The image from deconvolution interferometry provides a reliable representation of the structure in the model, whereas the correlation-based image is distorted by the dominant vibrational modes of the drill-bit source function. This model shows the feasibility of the passive application of drill-bit imaging in subsalt environments. Typically, SWD is not done in such environments because wells are deeper than they are onshore and transmission through the drill

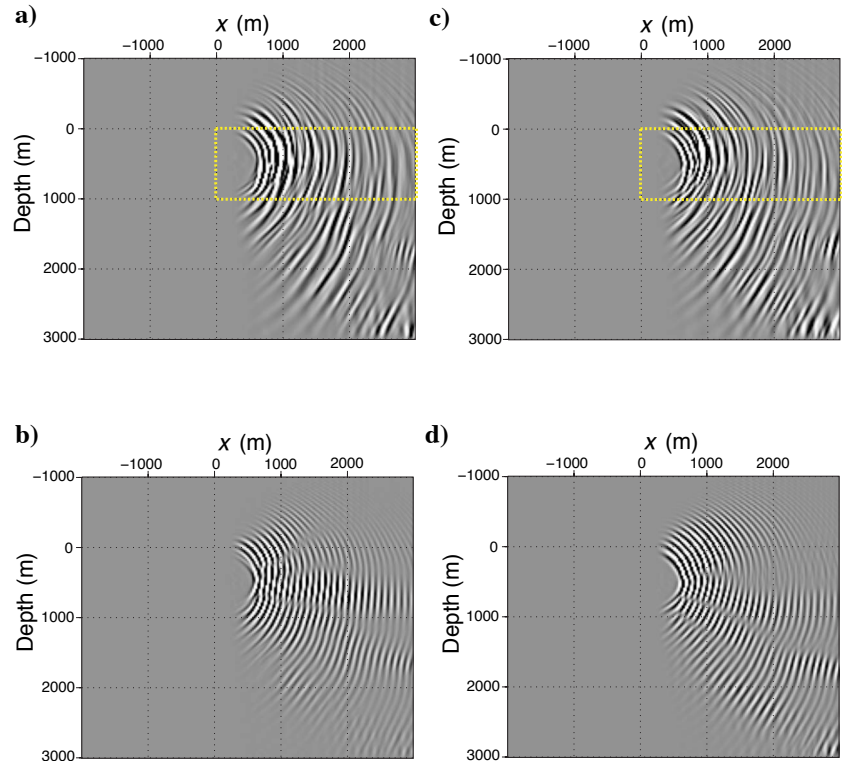


Figure 9. Shot-profile wave-equation images of interferometric shot gathers with a pseudosource at receiver 26. The left panels are the result of migrating pseudoshot gathers from deconvolution interferometry; the right panels result from crosscorrelation. Migration of data in Figure 7a and b yields panels (a) and (c), respectively. Panels (b) and (d) are obtained from migrating data in Figure 8a and b. Yellow boxes outline the subsurface area that is physically sampled by P-wave reflections. Data were migrated with the velocity model in Figure 5a.

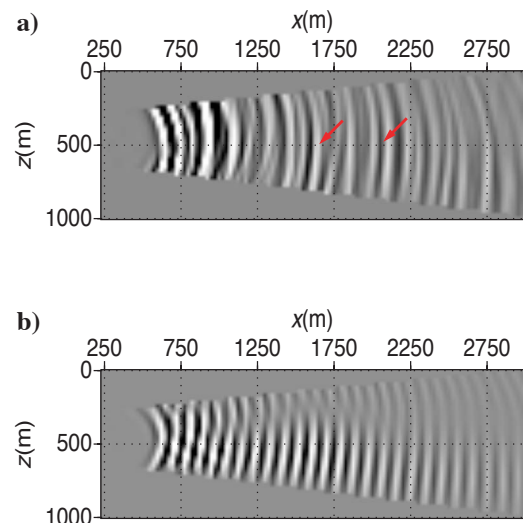


Figure 10. Final images from the interferometry of the SAFOD drill-bit noise recordings. (a) The result of stacking the images from deconvolution interferometry in Figure 9a and c. The right-hand arrow shows the location of the SAF reflector. The other arrow highlights the reflector associated to a blind fault zone at Parkfield. (b) The stack of images from correlation interferometry in Figure 9b and d. We muted the portion of the stacked images not representative of physical reflectors. The area of the image in (a) and (b) corresponds to the area bounded by yellow boxes in Figure 9.

string is weaker, which makes rig pilot records unreliable estimates of drill-bit excitation (Poletto and Miranda, 2004). Additionally, many subsalt wells are drilled with polycrystalline diamond compact (PDC) bits, which radiate less energy than roller-cone bits (Poletto, 2005a). The signal from PDC bits is thus difficult to measure from the surface or sea bottom. This difficulty can be overcome with downhole receiver arrays, as in our example.

Using field data acquired at the SAFOD pilot hole, we test the method of deconvolution interferometry for processing drill-bit noise records. The SAFOD SWD data are ideal for deconvolution interferometry because pilot recordings are not available. Single-scattered P-waves were obtained mostly by the deconvolution of the vertical component of recording of pilot-hole receivers with the vertical and northeast components of receiver 26. Shot-profile migration of interferometric shots generated by deconvolution yield coherent reflectors. From images presented here, along with active-shot data and fault intersection locations from the main hole, Vasconcelos et al. (2007) identify the SAF reflector as well as a (possibly active) blind fault at Parkfield. Their conclusions rely on the processing we describe here, in which interferometry by deconvolution plays an important role in imaging fault reflectors.

More than just an alternative to processing SWD data as they are acquired typically, deconvolution interferometry opens possibilities for using passive measurements of drill-bit or rig noise for imaging. The use of free-surface ghosts to reconstruct primary reflections that propagate between receivers (Schuster et al., 2003; Yu et al., 2004) is another example in which deconvolution interferometry can be applied. Interferometry of internal multiples potentially can be accomplished from SWD as well. The passive imaging from working drill bits could help monitor fields in environmentally sensitive areas, where active seismic experiments are limited. One such area is the

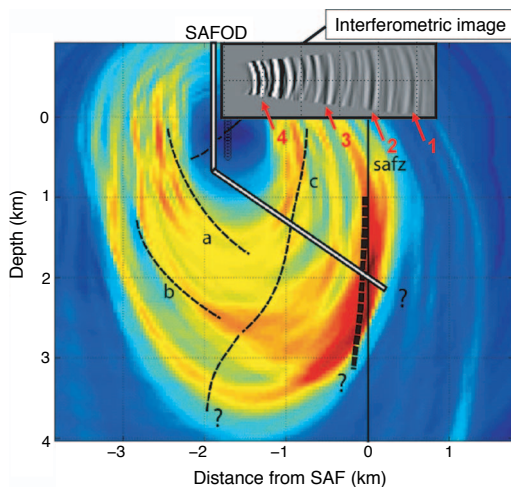


Figure 11. The deconvolution-based interferometric image in the context of the SAFOD. The image from deconvolution interferometry from Figure 10a (gray) is superposed on the image obtained by Chavarría et al. (2003). The color scheme indicates scattering strength (i.e., signal envelope); blue means no scattering and red means maximum scattering (Chavarría et al., 2003). The vertical solid black line indicates the lateral position of the surface trace of the SAF. The white line was the path predicted for the main hole at the time of publication of Chavarría et al. (2003). Dashed lines are possible faults interpreted by Chavarría et al. (2003). The interferometric image is displayed with opposite polarity with respect to that in Figure 10a to highlight the reflector that coincides with the surface trace of the SAF.

Tempa Rossa field in Italy (D'Andrea et al., 1993). Although active seismic experiments in this field are hindered by environmental regulations, its future production is expected to reach 50,000 barrels of oil per day. Environmentally friendly seismic monitoring of oil fields such as Tempa Rossa could be accomplished by applying deconvolution interferometry to recordings of the field's drilling activity.

CONCLUSION

We extend the deconvolution interferometry method to elastic media and show that it behaves in a manner analogous to the acoustic case described in Part 1. Elastic deconvolution interferometry can extract causal elastic scattered waves propagating between two receivers while suppressing arbitrarily complicated excitation functions. This comes at the cost of generating spurious arrivals caused by the clamped-point boundary condition imposed by deconvolution interferometry. We use interferometry by deconvolution as an alternative to processing SWD data. In these types of data sets, the signature of the drill-bit source function complicates the recovery of the subsurface response. Most SWD processing methods rely on the so-called pilot sensors to obtain an independent estimate of drill-bit excitation that is used to remove the drill-bit source function. Deconvolution interferometry can recover the subsurface response from SWD data without an independent estimate of drill-bit excitation. Additionally, knowledge about the drill-bit position is not a requirement for interferometry, as it is for other SWD applications. Interferometry requires, however, that the drill-bit sample the source stationary points that give rise to the target scattered waves.

ACKNOWLEDGMENTS

This research was financed by the National Science Foundation (grant EAS-0609595) and by the sponsors of the Consortium for Seismic Inverse Methods for Complex Structures at the Center for Wave Phenomena (CWP). Tom Taylor (Duke University; presently at Schlumberger) provided us with the SAFOD data, and his help was vital in identifying which portion of data could be used in our processing. Peter Malin (Duke University) gave us the orientations of pilot-hole receivers. The velocity model we used to migrate data was provided by Andres Chavarría (P/GSI). The equipment and acquisition of the SAFOD SWD data were donated by Schlumberger. We thank Flavio Poletto for visiting CWP during the 2006 Sponsor Meeting, when he kindly shared his expertise in drill-bit noise processing. Vasconcelos thanks Doug Miller and Jakob Haldorsen (both of Schlumberger) for discussions about SWD processing and deconvolution interferometry. We are thankful for reviews of Sergey Fomel, Art Weglein, Adriana Citali, and two anonymous reviewers.

APPENDIX A

CORRELATION REPRESENTATION THEOREM IN PERTURBED ELASTIC MEDIA

This derivation supports the argument that term 2 in equation 3 results in elastic scattered waves that propagate from \mathbf{r}_B to \mathbf{r}_A . Presented here is a special case of the derivation discussed in detail by Vasconcelos (2008), who derives representation theorems in perturbed media for generally linear operators that describe acoustic-

and elastic-wave phenomena in lossy moving media, quantum mechanical waves, electromagnetic phenomena, diffusion, flow, and advection.

Following Wapenaar and Fokkema (2004), perturbed and unperturbed elastic waves in lossless media can be described by the system of frequency-domain equations in matrix-vector form

$$\begin{aligned} i\omega\mathbf{A}\mathbf{u} + \mathbf{D}_r\mathbf{u} &= \mathbf{s} \\ i\omega\mathbf{A}_0\mathbf{u}_0 + \mathbf{D}_r\mathbf{u}_0 &= \mathbf{s}, \end{aligned} \quad (\text{A-1})$$

where $\mathbf{u}^T = \{\mathbf{v}^T, -\boldsymbol{\tau}_1^T, -\boldsymbol{\tau}_2^T, -\boldsymbol{\tau}_3^T\}$, with \mathbf{v} and $\boldsymbol{\tau}_i$ being observed particle velocity and traction vectors as a function of position \mathbf{r} . Subscript zero indicates unperturbed quantities; perturbed ones are $\mathbf{u} = \mathbf{u}_0 + \mathbf{u}_S$ and $\mathbf{A} = \mathbf{A}_0 + \mathbf{A}_S$, where subscript S represents perturbations. The source vector is given by $\mathbf{s}^T = \{\mathbf{f}^T, \mathbf{h}_1^T, \mathbf{h}_2^T, \mathbf{h}_3^T\}$, where \mathbf{f} and \mathbf{h}_i are force and deformation rate vectors. Matrices \mathbf{A} and \mathbf{A}_0 contain the spatially varying material parameters, such that $\mathbf{A} = \mathbf{C}^{-1}\bar{\mathbf{A}}$, with $\bar{\mathbf{A}} = \text{diag}\{\rho\mathbf{I}, \mathbf{I}, \mathbf{I}, \mathbf{I}\}$ (with ρ the spatially varying density and \mathbf{I} a 3×3 identity matrix) and

$$\mathbf{C} = \begin{pmatrix} \mathbf{I} & \mathbf{0} & \mathbf{0} & \mathbf{0} \\ \mathbf{0} & c_{11} & c_{12} & c_{13} \\ \mathbf{0} & c_{21} & c_{22} & c_{23} \\ \mathbf{0} & c_{31} & c_{32} & c_{33} \end{pmatrix}, \quad c_{jl} = \begin{pmatrix} c_{1j1l} & c_{1j2l} & c_{1j3l} \\ c_{2j1l} & c_{2j2l} & c_{2j3l} \\ c_{3j1l} & c_{3j2l} & c_{3j3l} \end{pmatrix}, \quad (\text{A-2})$$

where c_{ijkl} are the elements of the spatially varying stiffness tensor and $\mathbf{0}$ is a 3×3 null matrix.

The unperturbed matrix \mathbf{A}_0 is defined analogously with $\bar{\mathbf{A}}_0$ and \mathbf{C}_0 . The space-differentiation operator \mathbf{D}_r is defined as

$$\mathbf{D}_r = \begin{pmatrix} \mathbf{0} & \mathbf{D}_1 & \mathbf{D}_2 & \mathbf{D}_3 \\ \mathbf{D}_1 & \mathbf{0} & \mathbf{0} & \mathbf{0} \\ \mathbf{D}_2 & \mathbf{0} & \mathbf{0} & \mathbf{0} \\ \mathbf{D}_3 & \mathbf{0} & \mathbf{0} & \mathbf{0} \end{pmatrix}, \quad \mathbf{D}_j = \begin{pmatrix} \frac{\partial}{\partial r_j} & 0 & 0 \\ 0 & \frac{\partial}{\partial r_j} & 0 \\ 0 & 0 & \frac{\partial}{\partial r_j} \end{pmatrix}. \quad (\text{A-3})$$

For the system in equation A-1, it is possible to derive a correlation reciprocity theorem that relates unperturbed waves in a given wave state A with perturbed ones in state B (Vasconcelos, 2008). In the case considered here, such a theorem reads

$$\begin{aligned} \int_V \mathbf{s}_A^\dagger \mathbf{u}_{B,S} d^3\mathbf{r} &= \oint_{\partial V} \mathbf{u}_{A,0}^\dagger \mathbf{N}_r \mathbf{u}_{B,S} d^2\mathbf{r} + \int_V \mathbf{u}_{A,0}^\dagger \mathbf{V} \mathbf{u}_{B,S} d^3\mathbf{r} \\ &+ \int_V \mathbf{u}_{A,0}^\dagger \mathbf{V} \mathbf{u}_{B,0} d^3\mathbf{r}, \end{aligned} \quad (\text{A-4})$$

where \mathbf{N}_r is defined in the same way as \mathbf{D}_r (equation A-3) but with ∂_{r_j} replaced by n_j (the j -component of the vector normal to ∂V at \mathbf{r}) and $\mathbf{V} = i\omega(\mathbf{A} - \mathbf{A}_0)$ is the *scattering potential* (e.g., Born and Wolf, 1959; Rodberg and Thaler, 1967). Subscripts A and B indicate whether the fields are observed in states A or B . Superscript \dagger represents the adjoint, i.e., the conjugate-transpose matrix. The Green's matrix-vector form of equation A-4 can be obtained by setting \mathbf{s}_A^T

$= \delta(\mathbf{r} - \mathbf{r}_A)\{\mathbf{1}^T, \mathbf{1}^T, \mathbf{1}^T, \mathbf{1}^T\}$ (where $\mathbf{1}$ is a unitary vector), $\mathbf{u}_{A,B} = \mathbf{G}(\mathbf{r}_{A,B}, \mathbf{r})$, and $\mathbf{u}_0 = \mathbf{G}_0(\mathbf{r}_{A,B}, \mathbf{r})$. This results in

$$\begin{aligned} \mathbf{G}_S(\mathbf{r}_A, \mathbf{r}_B) &= \oint_{\partial V} \mathbf{G}_0^\dagger(\mathbf{r}_A, \mathbf{r}) \mathbf{N}_r \mathbf{G}_S(\mathbf{r}_B, \mathbf{r}) d^2\mathbf{r} \\ &+ \int_V \mathbf{G}_0^\dagger(\mathbf{r}_A, \mathbf{r}) \mathbf{V} \mathbf{G}_S(\mathbf{r}_B, \mathbf{r}) d^3\mathbf{r} \\ &+ \int_V \mathbf{G}_0^\dagger(\mathbf{r}_A, \mathbf{r}) \mathbf{V} \mathbf{G}_0(\mathbf{r}_B, \mathbf{r}) d^3\mathbf{r}. \end{aligned} \quad (\text{A-5})$$

This representation theorem shows that the desired scattered fields $\mathbf{G}_S(\mathbf{r}_B, \mathbf{r}_A)$ can be retrieved by crosscorrelations between unperturbed waves measured at \mathbf{r}_A and unperturbed waves and field perturbations observed at \mathbf{r}_B . Equation A-5 is impractical for seismic interferometry because the evaluation of the volume integrals requires knowledge of the spatially varying medium parameters to compute \mathbf{V} . Generally, the volume integrals in equation A-5 cannot be neglected. However, if the scatterers are located away from both \mathbf{r}_A and \mathbf{r}_B in the same configuration described by Figure A-1 of Part 1, then

$$\mathbf{G}_S(\mathbf{r}_A, \mathbf{r}_B) \approx \int_{\partial V_1} \mathbf{G}_0^\dagger(\mathbf{r}_A, \mathbf{r}) \mathbf{N}_r \mathbf{G}_S(\mathbf{r}_B, \mathbf{r}) d^2\mathbf{r} \quad (\text{A-6})$$

after Vasconcelos (2008). The value ∂V_1 is a segment of ∂V that contains stationary source points contributing to $\mathbf{G}_S(\mathbf{r}_A, \mathbf{r}_B)$. For $\mathbf{r} \in \partial V_1$, the scattering potential \mathbf{V} is a null matrix along the stationary paths of unperturbed waves in the integrand on the third line of equation A-5. Thus, the contribution of the second volume integral in equation A-5 is zero. In the special case described by Figure A-1 of Part 1, the contribution of the first volume integral in equation A-5 has the same phase as that of the surface integral, but the volume integral contribution is weaker because it is of higher order in \mathbf{V} .

From equation A-6, the p -component of the particle velocity response v because of a point-force f oriented in the q -direction is given by

$$\begin{aligned} G_{S(p,q)}^{(v,f)}(\mathbf{r}_A, \mathbf{r}_B) &\approx \int_{\partial V_1} [G_{S(p,ij)}^{(v,h)}(\mathbf{r}_A, \mathbf{r}) \{G_{0(q,i)}^{(v,f)}(\mathbf{r}_B, \mathbf{r})\}^*] n_j ds \\ &+ \int_{\partial V_1} [\{G_{0(p,ij)}^{(v,h)}(\mathbf{r}_B, \mathbf{r})\}^* G_{S(q,i)}^{(v,f)}(\mathbf{r}_A, \mathbf{r})] n_j ds, \end{aligned} \quad (\text{A-7})$$

where ij are components of the deformation-rate sources h .

Because the formulation with deformation-rate sources is impractical for interferometry, we assume the medium at and outside ∂V is homogeneous, isotropic, and unperturbed (after Figure A-1 in Part 1). Then using the transformation proposed by Wapenaar and Fokkema (2006), we get

$$\begin{aligned} G_{S(p,q)}^{(v,f)}(\mathbf{r}_A, \mathbf{r}_B) &\approx \int_{\partial V_1} \frac{2}{i\omega\rho} G_{S(p,K)}^{(v,\Phi)}(\mathbf{r}_A, \mathbf{r}) \\ &\times \{\partial_i G_{0(q,K)}^{(v,\Phi)}(\mathbf{r}_B, \mathbf{r})\}^* n_j ds, \end{aligned} \quad (\text{A-8})$$

where Φ denotes sources that are either P-wave sources with $K = 0$ or differently oriented S-wave sources with $K = 1, 2, 3$. As in equa-

tion 1, equation A-8 assumes a summation over the source index K .

Because the space derivatives $\partial_i G$ typically are not measured in seismic surveys, we approximate the dipole sources in equation A-8 by monopole sources by imposing the radiation boundary condition $\partial_i G_{(q,K)}^{(v,\Phi)} = -i\omega c_K^{-1} G_{(q,K)}^{(v,\Phi)}$ (Wapenaar and Fokkema, 2006). This yields

$$G_{S(p,q)}^{(v,f)}(\mathbf{r}_A, \mathbf{r}_B) \approx \frac{2}{\rho c_K} \int_{\partial V_1} G_{S(p,K)}^{(v,\Phi)}(\mathbf{r}_A, \mathbf{r}) \{G_{0(q,K)}^{(v,\Phi)}(\mathbf{r}_B, \mathbf{r})\}^* ds, \quad (\text{A-9})$$

with c_K equal to c_P (the P-wave velocity at ∂V) for $K = 0$ and equal to c_S (the S-wave velocity at ∂V) for $K = 1, 2, 3$. Equation A-9 retrieves the p -component of the elastic scattered-wave response at \mathbf{r}_B because of a q -oriented pseudoforce at \mathbf{r}_B . This is accomplished by crosscorrelating the p -component of scattered waves observed at \mathbf{r}_A with unperturbed waves observed at \mathbf{r}_B . These correlations are summed for all source types and source positions to give the desired scattered-wave response. Equation A-9 justifies our interpretation that term 2 in equation 3 results in elastic scattered waves (equation 4).

APPENDIX B

SHORT NOTE ON DECONVOLUTION

Our numerical implementation of deconvolution is based on the so-called water-level deconvolution (Clayton and Wiggins, 1976), given by

$$D_{AB} = \frac{u(\mathbf{r}_A, \mathbf{s})}{u(\mathbf{r}_B, \mathbf{s})} \approx \frac{u(\mathbf{r}_A, \mathbf{s})u^*(\mathbf{r}_B, \mathbf{s})}{|u(\mathbf{r}_B, \mathbf{s})|^2 + \varepsilon \langle |u(\mathbf{r}_B, \mathbf{s})|^2 \rangle}, \quad (\text{B-1})$$

where $\langle |u(\mathbf{r}_B, \mathbf{s})|^2 \rangle$ is the average of the power spectrum of data measured at \mathbf{r}_B . Factor ε is a free parameter that we choose by visually inspecting the output of the deconvolution in equation B-1. When ε is too large, the denominator becomes a constant and the result of the deconvolution approximates the result of crosscorrelation (equation 7). When ε is too small, the deconvolution becomes unstable. An optimal value of ε results in the desired deconvolved trace, with weak random noise associated with water-level regularization (Clayton and Wiggins, 1976).

Other deconvolution approaches can yield better results than the water-level deconvolution method. For deconvolution references in exploration geophysics literature, we refer to the collection edited by Webster (1978) and work of Porsani and Ursin (2000, 2007). In the signal-processing field, the work of Bennis and Nahman (1990) and Qu et al. (2006) are examples of deconvolution methods relevant to SWD processing.

REFERENCES

- Aki, K., and P. G. Richards, 1980, Quantitative seismology: W. H. Freeman & Co.
- Armstrong, P., L. Nutt, and R. Minton, 2000, Drilling optimization using drill-bit seismic in the deepwater Gulf of Mexico: Presented at the International Association of Drilling Contractors/Society of Petroleum Engineers Drilling Conference, IADC/SPE 59222.
- Bakulin, A., and R. Calvert, 2006, The virtual source method: Theory and case study: *Geophysics*, **71**, no. 4, S1139–S1150.
- Bennis, A., and N. S. Nahman, 1990, Deconvolution of causal pulse and transient data: *IEEE Transactions on Instrumentation and Measurement*, **39**, 933–939.
- Boness, N. L., and M. D. Zoback, 2006, A multiscale study of the mechanisms controlling shear velocity anisotropy in the San Andreas Fault Observatory at Depth: *Geophysics*, **71**, no. 5, F131–F146.
- Born, M., and E. Wolf, 1959, Principles of optics: Cambridge University Press.
- Chavarría, J. A., P. Malin, R. D. Catchings, and E. Shalev, 2003, A look inside the San Andreas fault at Parkfield through vertical seismic profiling: *Science*, **302**, 1746–1748.
- Claerbout, J. F., 1985, Imaging the earth's interior: Blackwell Scientific Publications, Inc.
- Clayton, R. W., and R. A. Wiggins, 1976, Source shape estimation and deconvolution of teleseismic body waves: *Geophysical Journal of the Royal Astronomical Society*, **47**, 151–177.
- D'Andrea, S., R. Pasi, G. Bertozzi, and P. Dattilo, 1993, Geological model, advanced methods help unlock oil in Italy's Apennines: *Oil & Gas Journal*, **91**, 53–57.
- Draganov, D., K. Wapenaar, and J. Thorbecke, 2006, Seismic interferometry: Reconstructing the earth's reflection response: *Geophysics*, **71**, no. 4, S161–S170.
- Haldorsen, J. B. U., D. E. Miller, and J. J. Walsh, 1994, Walk-away VSP using drill noise as a source: *Geophysics*, **60**, 978–997.
- Larose, E., L. Margerin, A. Derode, B. van Tiggelen, M. Campillo, N. Shapiro, A. Paul, L. Stehly, and M. Tanter, 2006, Correlation of random wavefields: An interdisciplinary review: *Geophysics*, **71**, no. 4, S111–S121.
- Malusa, M., F. Poletto, and F. Miranda, 2002, Prediction ahead of the bit by using drill-bit pilot signals and reverse vertical seismic profiling (RVSP): *Geophysics*, **67**, 1169–1176.
- Miller, D., J. Haldorsen, and C. Kostov, 1990, Methods for deconvolution of unknown source signatures from unknown waveform data: U.S. Patent 4 922 362.
- Poletto, F., 2005a, Energy balance of a drill-bit seismic source, Part 1: Rotary energy and radiation properties: *Geophysics*, **70**, no. 2, T13–T28.
- , 2005b, Energy balance of a drill-bit seismic source, Part 2: Drill bit versus conventional seismic sources: *Geophysics*, **70**, no. 2, T29–T44.
- Poletto, F., M. Malusa, F. Miranda, and U. Tinivella, 2004, Seismic-while-drilling by using dual sensors in drill strings: *Geophysics*, **69**, 1261–1271.
- Poletto, F., and F. Miranda, 2004, Seismic while drilling, fundamentals of drill-bit seismic for exploration: SEG.
- Poletto, F., and L. Petronio, 2006, Seismic interferometry with a TBM source of transmitted and reflected waves: *Geophysics*, **71**, no. 4, S185–S193.
- Poletto, F., F. L. Rocca, and L. Bertelli, 2000, Drill-bit signal separation for RVSP using statistical independence: *Geophysics*, **65**, 1654–1659.
- Porsani, M., and B. Ursin, 2000, Mixed-phase deconvolution and wavelet estimation: *The Leading Edge*, **19**, 76–79.
- , 2007, Direct multichannel predictive deconvolution: *Geophysics*, **72**, no. 2, H11–H27.
- Qu, L., P. S. Routh, and K. Ko, 2006, Wavelet deconvolution in a periodic setting using cross-validation: *IEEE Signal Processing Letters*, **13**, 232–235.
- Rector, J. W., 1992, Noise characterization and attenuation in drill bit recordings: *Journal of Seismic Exploration*, **1**, 379–393.
- Rector, J. W., and B. A. Hardage, 1992, Radiation pattern and seismic waves generated by a working roller-cone drill bit: *Geophysics*, **57**, 1319–1333.
- Rector, J. W., and B. P. Marion, 1991, The use of drill-bit energy as a down-hole seismic source: *Geophysics*, **56**, 628–634.
- Rodberg, L. S., and R. M. Thaler, 1967, Introduction to the quantum theory of scattering: Academic Press Inc.
- Schuster, G. T., F. Followill, L. J. Katz, J. Yu, and Z. Liu, 2004, Autocorrelation migration: Theory: *Geophysics*, **68**, 1685–1694.
- Snieder, R., J. Sheiman, and R. Calvert, 2006, Equivalence of the virtual-source method and wave-field deconvolution in seismic interferometry: *Physical Review E*, **73**, 066620.
- Snieder, R., K. Wapenaar, and K. Lerner, 2006, Spurious multiples in seismic interferometry of primaries: *Geophysics*, **71**, no. 4, S1111–S1124.
- Snieder, R., K. Wapenaar, and U. Wegler, 2007, Unified Green's function retrieval by cross-correlation: Connection with energy principles: *Physical Review E*, **75**, 036103.
- Solum, J. G., S. H. Hickman, D. A. Lockner, D. E. Moore, B. A. van der Pluijm, A. M. Schleicher, and J. P. Evans, 2006, Mineralogical characterization of protolith and fault rocks from the SAFOD main hole: *Geophysical Research Letters*, **33**, L21314.
- Tsvankin, I., 2001, Seismic signatures and analysis of reflection data in anisotropic media: Elsevier Science Publ. Co., Inc.
- Vasconcelos, I., 2007, Interferometry in perturbed media: Ph.D. dissertation, Colorado School of Mines.
- , 2008, Perturbation-based interferometry — Applications and connection to seismic imaging: 70th Annual Conference and Exhibition, EAGE, Extended Abstracts.
- Vasconcelos, I., and R. Snieder, 2008, Interferometry by deconvolution, Part 1 — Theory for acoustic waves and numerical examples: *Geophysics*, **73**, no. 3, S115–S128.
- Vasconcelos, I., S. T. Taylor, R. Snieder, J. A. Chavarría, P. Sava, and P. Ma-

- lin, 2007, Broadside interferometric and reverse-time imaging of the San Andreas fault at depth: 77th Annual International Meeting, SEG, Expanded Abstracts, 2175–2179.
- Wapenaar, K., 2004, Retrieving the elastodynamic Green's function of an arbitrary inhomogeneous medium by cross correlation: *Physical Review Letters*, **93**, 254301.
- , 2006, Green's function retrieval by cross-correlation in case of one-sided illumination: *Geophysical Research Letters*, **33**, L19304.
- , 2007, General representations for wavefield modeling and inversion in geophysics: *Geophysics*, **72**, no. 5, SM5–SM17.
- Wapenaar, K., and J. Fokkema, 2004, Reciprocity theorems for diffusion, flow and waves: *Journal of Applied Mechanics*, **71**, 145–150.
- , 2006, Green's function representations for seismic interferometry: *Geophysics*, **71**, no. 4, S1133–S1146.
- Webster, G. M., 1978, *Deconvolution: SEG*.
- Yu, J., L. J. Katz, F. Followill, H. Sun, and G. T. Schuster, 2004, Autocorrelation migration: IVSPWD test: *Geophysics*, **68**, 297–307.